Inorg. Chem. **2009**, *48*, 2549−2560

Structural, Spectroscopic, and Thermodynamic Consequences of Anti-Chelate Effect in Nine-Coordinate Lanthanide Podates

Patrick E. Ryan,[†] Laure Guénée,[†] Gabriel Canard,[‡] Frédéric Gumy,[§] Jean-Claude G. Bünzli,[§] and Claude Piguet*[,†]

Department of Inorganic, Analytical and Applied Chemistry, University of Geneva, 30 quai E. Ansermet, CH-1211 Geneva 4, Switzerland, Institut des Sciences Moléculaires de Marseille, CNRS UMR 6263, Aix-Marseille University, Avenue escadrille Normandie-Niemen, F-13397 Marseille Cedex 20, France, and Laboratory of Lanthanide Supramolecular Chemistry, École Polytechnique Fédérale de Lausanne, BCH 1402, CH-1015 Lausanne, Switzerland

Received November 7, 2008

The connection of three tridentate 2,6-bis(1-ethyl-benzimidazol-2-yl)pyridine binding units to an extended sulfur-containing tripodal anchor in the ligand **L9** yields nine-coordinate podates $[Ln(\mathbf{L9})]^{3+}$ upon reaction with trivalent lanthanides, Ln(III). Structural analysis of $[Eu(\mathbf{L9})](ClO_4)_3$ in the solid state with the help of the bond valence method shows that the peripheral ethyl groups are responsible for a specific distortion of the triple-helical structure, which allows a closer approach of the nitrogen donors toward the central metal, while minimizing interstrand repulsion. The consequences of this distortion on the Eu(III) luminescent probe are investigated by high-resolution emission spectroscopy, while paramagnetic NMR data collected in acetonitrile demonstrate that $[Ln(\mathbf{L9})]^{3+}$ adopts a single relaxed C_3-symmetrical structure along the complete lanthanide series. The persistence of the triple-helical structure in solution is obtained at the cost of severe constraints in the helically wrapped organic tripod, which strongly disfavor intramolecular cyclization processes. The resulting antichelate effect can be exploited for the selective preparation of polynuclear complexes with tripodal ligands.

Introduction

According to classical textbooks in coordination chemistry,[1,2] the connection of several binding units in a multidentate ligand is at the origin of the chelate effect, which stabilizes the final metallic complexes, mainly for entropic reasons. This favorable contribution has been systematically exploited during the past five decades for improving the stability and kinetic inertness of trivalent lanthanide complexes,[3−5] thus allowing their recent successful applications as MRI contrast agents[6−11] and luminescent sensors[12−17] in biological media. Though often invoked, the chelate effect is rarely explicitly quantified in lanthanide coordination

* To whom correspondence should be addressed. E-mail: Claude.Piguet@unige.ch.
† University of Geneva.
‡ Aix-Marseille University.
§ École Polytechnique Fédérale de Lausanne.

(1) Purcell, K. F.; Kotz, J. C. *Inorganic Chemistry*; W.B. Saunders Company: Philadelphia, PA, 1977; p 739.
(2) Cotton, F. A.; Wilkinson, G. *Advanced Inorganic Chemistry*, 4th ed.; John Wiley & Sons: New York, 1980; p 71.
(3) Bünzli, J.-C. G. In *Rare Earths*; Saez-Puche, R., Caro, P. A., Eds.; Editorial Complutense: Madrid, 1998; pp 223−259.
(4) Piguet, C.; Bünzli, J.-C. G. *Chem. Soc. Rev.* **1999**, *28*, 347–358.
(5) Cotton, S. *Lanthanide and Actinide Chemistry*; John Wiley & Sons, Ltd: Chichester, U.K., 2006.
(6) Aime, S.; Botta, M.; Fasano, M.; Terreno, E. *Chem. Soc. Rev.* **1998**, *27*, 19–29.
(7) Caravan, P.; Ellison, J. J.; McMurry, T. J.; Lauffer, R. B. *Chem. Rev.* **1999**, *99*, 2293–2352.
(8) Caravan, P. *Chem. Soc. Rev.* **2006**, *35*, 512–523.
(9) Bottrill, M.; Kwok, L.; Long, N. J. *Chem. Soc. Rev.* **2006**, *35*, 557–571.
(10) Chan, K. W.-Y.; Wong, W.-T. *Coord. Chem. Rev.* **2007**, *251*, 2428–2451.
(11) Hermann, P.; Kotek, J.; Kubicek, V.; Lukes, I. *Dalton Trans.* **2008**, 3027–3047.
(12) Petoud, S.; Cohen, S. M.; Bünzli, J.-C. G.; Raymond, K. N. *J. Am. Chem. Soc.* **2003**, *125*, 13324–13325.
(13) Johansson, M., K.; Cook, R. M.; Xu, J.; Raymond, K. N. *J. Am. Chem. Soc.* **2004**, *126*, 16451–16455.
(14) Petoud, S.; Muller, G.; Moore, E. G.; Xu, J.; Sokolnicki, J.; Riehl, J. P.; Le, U. N.; Cohen, S. M.; Raymond, K. N. *J. Am. Chem. Soc.* **2007**, *129*, 77–83.
(15) Nishioka, T.; Fukui, K.; Matsumoto, K. In *Handbook on the Physics and Chemistry of Rare Earths*; Gschneidner, K. A., Jr., Bünzli, J.-C. G., Pecharsky, V. K., Eds.; Elsevier Science: Amsterdam, 2007; Vol. 37, pp 171−220.
(16) Parker, D. *Chem. Soc. Rev.* **2004**, *33*, 156–165.
(17) Gunnlaugsson, T.; Leonard, J. P. *Chem. Commun.* **2005**, 3114–3131.

10.1021/ic802130z CCC: $40.75
Published on Web 02/13/2009

Chart 1

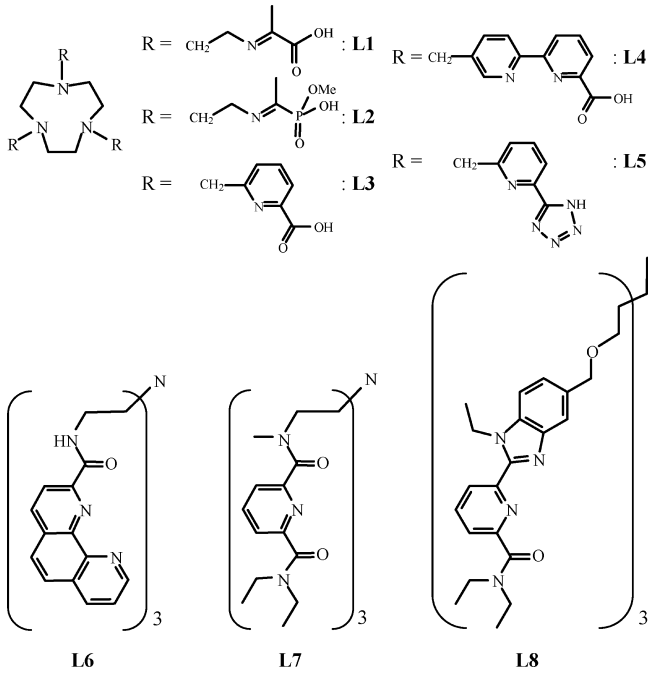

chemistry,[18] but chemists are usually confident in its constant help for stabilizing their favored complexes. In this context, the covalent connection of three tridentate binding units to a single anchor in ligands **L1**−**L8** matches the classical strategy for producing stable and saturated nine-coordinate triple-helical lanthanide podates [Ln(**L*k***-3H)] ($k = 1-4$)[19−22] or $[Ln(\mathbf{L}k)]^{3+}$ ($k = 5-8$; Chart 1).[23−26]

Despite the intriguing and recurrent enormous gap observed between the free energies of formation of the podates $[Ln(\mathbf{L}k)]^{3+}$ ($-47 \le \Delta G_{1,1}^{Ln,Lk} \le -37$ kJ/mol for $k = 6-8$, Chart 1)[24−26] and those of their parent triple-helical complexes $[Ln(\mathbf{L}k)_3]^{3+}$ ($-133 \le \Delta G_{1,3}^{Ln,Lk} \le -97$ kJ/mol for $k = 10-12$, Chart 2)[27,28] in acetonitrile, the quantitative estimation of the chelate effect brought by the covalent tripod in these systems has been only recently addressed for the related ligand **L9** (Chart 2).[27] The application of the site-binding model to $[Ln(\mathbf{L9})]^{3+}$ ($-46 \le \Delta G_{1,1}^{Ln,L9} \le -41$ kJ/mol for Ln = La−Lu) and $[Ln(\mathbf{L11})]^{3+}$ assigned this striking antichelate effect to a disastrous preorganization of the tridentate binding units by the extended sulfur-containing tripod in acetonitrile, which drastically limits intramolecular cyclization processes.[27] We calculated that the intermolecular free energy of connection of the first tridentate N_3 binding unit of the tripodal ligand **L9** logically becomes more negative along the lanthanide series (-35 (Ln = La) $\ge \Delta G_{conn,N3}^{inter} \ge -52$ kJ/mol (Ln = Lu); Figure 1) but that the two subsequent intramolecular binding events leading to the C_3-symmetrical nine-coordinate podates $[Ln(\mathbf{L9})]^{3+}$ only contribute to $\Delta G_{conn,N3}^{intra} = -8$ kJ/mol because of severe enthalpic limitations assigned to unfavorable strain energy (Figure 1).[27]

Chart 2

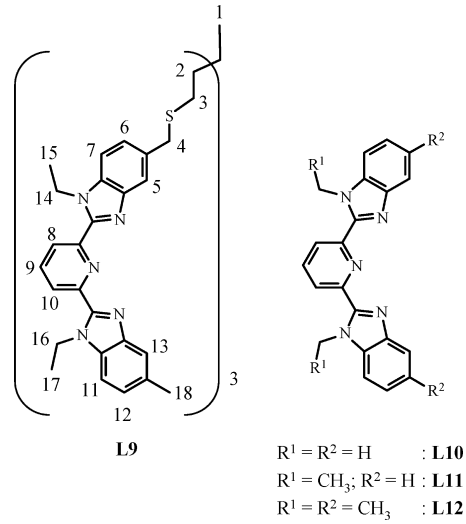

Consequently, the stability constants of the podates ($7.2 \le \log(\beta_{1,3}^{Ln,Lk}) \le 8.0$)[27] are reduced by more than 10 orders of magnitude when they are compared with those obtained for the triple-helical complexes $[Ln(\mathbf{L}k)_3]^{3+}$ ($k = 10-12$, $17 \le \log(\beta_{1,3}^{Ln,Lk}) \le 23$ for Ln = La−Lu),[27−29] in which purely intermolecular complexation processes are involved. In our quest for novel concepts aiming at controlling nuclearity, structure, and selectivity in lanthanide coordination chemistry, we propose in this contribution a thorough exploration of the origin and structural, electronic, and thermodynamic consequences of the drastic antichelate effect operating in $[Ln(\mathbf{L9})]^{3+}$.

Results and Discussion

Solid-State Structure and Bond Valence Analysis. The crystal structure of $[Eu(\mathbf{L9})](ClO_4)_3 \cdot 2CH_3CN \cdot C_2H_5OH \cdot 0.5H_2O$ has been previously reported (Figure 2c).[27] The geometrical analysis of the molecular structure of the cation $[Eu(\mathbf{L9})]^{3+}$ leads to the following conclusions: (1) The three helically wrapped and coordinated tridentate 2,6-bis(1-ethylbenzimidazol-2-yl)pyridine units display a pseudo-3-fold symmetry with a larger distortion for strand B, while the alkyl chains of the organic tripod severely deviate from C_3 symmetry (Figure 2c). (2) The metric of the pseudo-tricapped trigonal prismatic EuN_9 coordination sphere is similar in $[Eu(\mathbf{L9})]^{3+}$ and in $[Eu(\mathbf{L12})_3]^{3+}$. (3) The close packing of

(18) Caravan, P.; Mehrkhodavandi, P.; Orvig, C. *Inorg. Chem.* **1997**, *36*, 1316–1321.
(19) Tei, L.; Baum, G.; Blake, A. J.; Fenske, D.; Schröder, M. *J. Chem. Soc., Dalton Trans.* **2000**, 2793–2799.
(20) Tei, L.; Blake, A. J.; Wilson, C.; Schröder, M. *Dalton Trans.* **2004**, 1945–1952.
(21) Gateau, C.; Mazzanti, M.; Pécaut, J.; Dunand, F. A.; Helm, L. *Dalton Trans.* **2003**, 2428–2433.
(22) Charbonnière, L. J.; Ziessel, R.; Guardigli, M.; Roda, A.; Sabbatini, N.; Cesario, M. *J. Am. Chem. Soc.* **2001**, *123*, 2436–2437.
(23) Giraud, M.; Andreiadis, E. S.; Fisyuk, A. S.; Demadrille, R.; Pécaut, J.; Imbert, D.; Mazzanti, M. *Inorg. Chem.* **2008**, *47*, 3952–3964.
(24) Bretonnière, Y.; Wietzke, R.; Lebrun, C.; Mazzanti, M.; Pécaut, J. *Inorg. Chem.* **2000**, *39*, 3499–3505.
(25) Renaud, F.; Piguet, C.; Bernardinelli, G.; Bünzli, J.-C. G.; Hopfgartner, G. *J. Am. Chem. Soc.* **1999**, *121*, 9326–9342.
(26) Koeller, S.; Bernardinelli, G.; Piguet, C. *Dalton Trans.* **2003**, 2395–2404.
(27) Canard, G.; Koeller, S.; Bernardinelli, G.; Piguet, C. *J. Am. Chem. Soc.* **2008**, *130*, 1025–1040.
(28) Petoud, S.; Bünzli, J.-C. G.; Renaud, F.; Piguet, C.; Schenk, K. J.; Hopfgartner, G. *Inorg. Chem.* **1997**, *36*, 5750–5760.
(29) Piguet, C.; Bünzli, J.-C. G.; Bernardinelli, G.; Bochet, C. G.; Froidevaux, P. *J. Chem. Soc., Dalton Trans.* **1995**, 83–97.

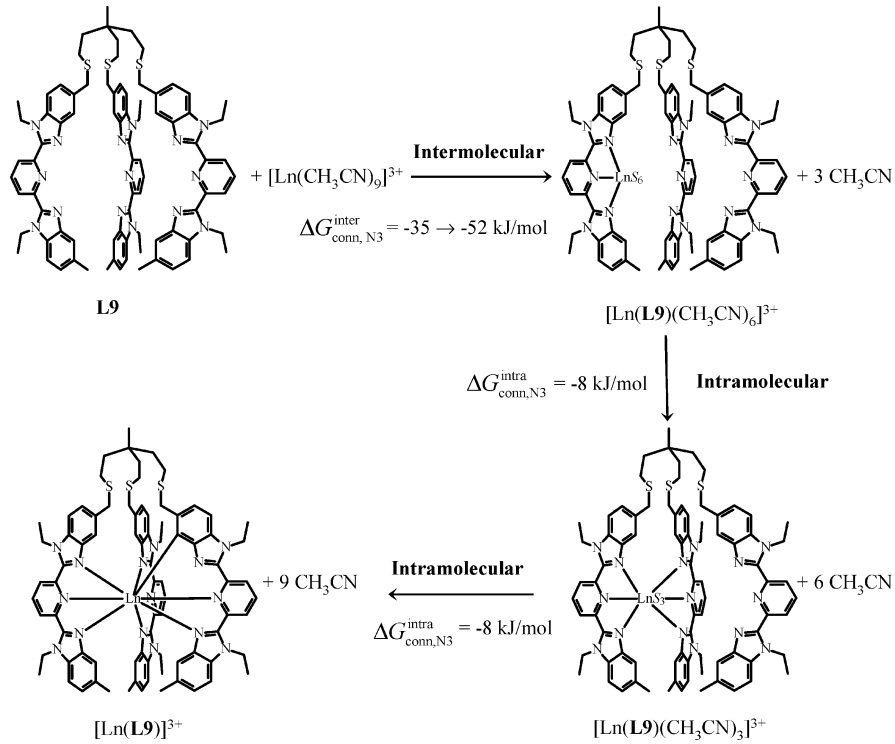

Figure 1. Successive complexation reactions leading to $[Ln(\mathbf{L9})]^{3+}$ and their thermodynamic characteristics in acetonitrile (298 K).[27]

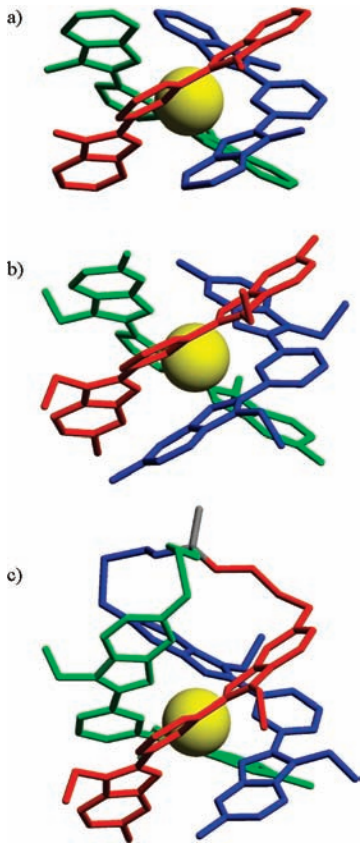

Figure 2. Perspective views of the molecular structures of (a) $[Eu(\mathbf{L10})_3]^{3+}$,[30] (b) $[Eu(\mathbf{L12})_3]^{3+}$,[29] and $[Eu(\mathbf{L9})]^{3+}$,[27] in the solid state showing the close packing of the aromatic tridentate binding units (strand A = blue, strand B = green, strand C = red).

the aromatic rings of the different strands A, B, and C along the pseudo-3-fold axis produces two significant intramolecular interstrand π-stacking interactions (bzimA−bzimB and pyB−bzimC, bzim = benzimidazole, py = pyridine). A further closer scrutiny at the organization of the strands indicates that the lack of significant interactions between strands A anb C results from the slide of these strands in opposite directions. Compared with the nonchelated tridentate binding units in the complex $[Eu(\mathbf{L}k)_3]^{3+}$ (k = 10, 12), we indeed notice that a related trend is observed on going from $[Eu(\mathbf{L10})_3]^{3+}$ (R^1 = H, Chart 2: existence of a C_3-crystallographic axis shown in Figure 2a)[30] to $[Eu(\mathbf{L12})_3]^{3+}$ (R^1 = CH_3, Chart 2: loss of the C_3-crystallographic axis due to the opposite slide of strands A and C shown in Figure 2b).[29] We conclude that this distortion minimizes the intramolecular interstrand repulsion between ethyl groups bound to closely packed benzimidazole rings belonging to different strands in $[Eu(\mathbf{L9})]^{3+}$ and $[Eu(\mathbf{L12})_3]^{3+}$.

The precise organization of the three strands affects the global interaction of the nine N-donor atoms with Eu(III), which can be quantified by using the bond valence method.[31−33] Assuming that the bond valence ($\nu_{Eu,j}$) of an interacting nitrogen donor j in the first coordination sphere located at a distance $d_{Eu,j}$ from the metal is given by the usual eq 1 ($R_{Eu,j}$ is known as the bond valence parameter, which only depends on the pair of interacting atoms and amounts to 2.161 Å for Eu−N interactions,[34] and b = 0.37 Å is a

(30) Piguet, C.; Bünzli, J.-C. G.; Bernardinelli, G.; Williams, A. F. *Inorg. Chem.* **1993**, *32*, 4139–4149.
(31) Brown, I. D.; Altermatt, D. *Acta Crystallogr., Sect. B* **1985**, *B41*, 244–247.
(32) Brese, N. E.; O'Keeffe, M. *Acta Crystallogr., Sect. B* **1991**, *B47*, 192–197.
(33) Brown, I. D. *Acta Crystallogr., Sect. B* **1992**, *B48*, 553–572.
(34) Trzesowska, A.; Kruszynski, R.; Bartczak, T. J. *Acta Crystallogr., Sect. B* **2005**, *B61*, 429–434.

Chart 3

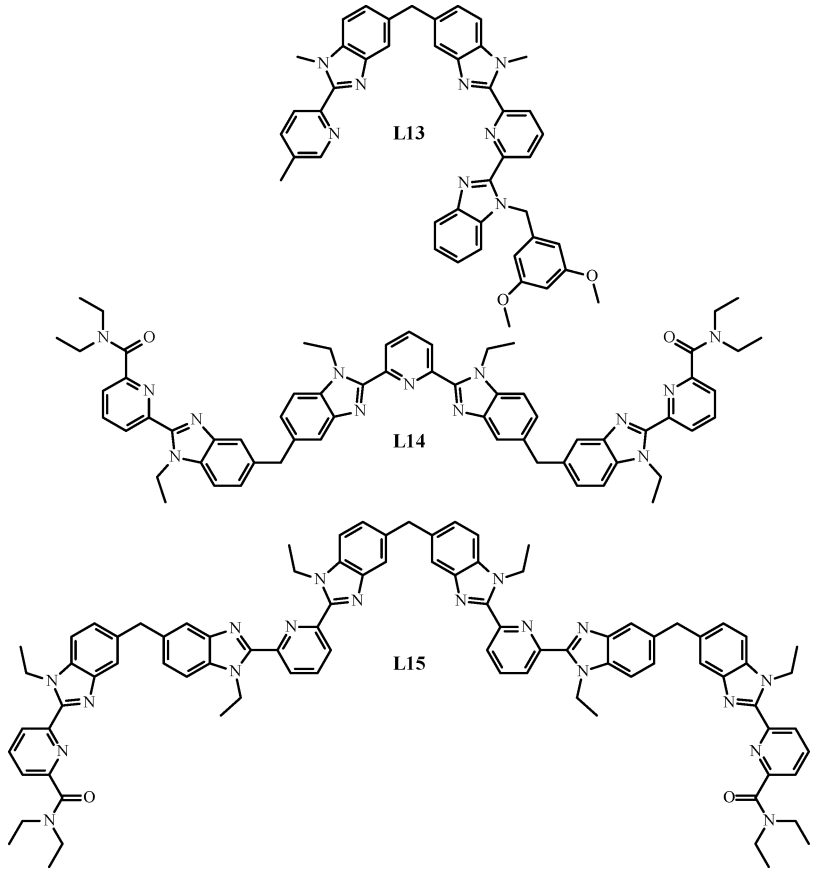

scaling constant),[31] the total bond valence of the europium atom V_{Eu} can be calculated with eq 2 (Tables S1−S3, Supporting Information).

$$\nu_{Eu,j} = e^{(R_{Eu,j} - d_{Eu,j})/b} \quad (1)$$

$$V_{Eu} = \sum_j \nu_{Eu,j} \quad (2)$$

The stepwise increase of $V_{Eu} = 2.80$ ($[Eu(\mathbf{L10})_3]^{3+}$) toward $V_{Eu} = 2.84$ ($[Eu(\mathbf{L12})_3]^{3+}$) and $V_{Eu} = 2.90$ ($[Eu(\mathbf{L9})]^{3+}$) for the same EuN_9 site agrees with the increasing slide of strands A and C evidenced in the geometrical analysis of the coordination sphere of these complexes.[27,29] Interestingly, larger values of V_{Eu} imply improved Eu−N(heterocyclic) interactions because the Eu−N bond lengths are slightly reduced by the slide of the strands, which leads to the relaxation of the intramolecular interstrand π-stacking interactions. We thus deduce that the latter stabilizing interactions evidenced in the crystal structure of $[Eu(\mathbf{L10})_3]^{3+}$ are obtained at the cost of a slight increase of the Eu−N bonds.[30]

Solid-State Structure and Photophysical Properties. The unusual photophysical characteristics of the pseudo-tricapped trigonal prismatic EuN_9 site found in $[Eu(\mathbf{L10})_3]^{3+}$ and $[Eu(\mathbf{L12})_3]^{3+}$ have been the subject of intense research,[29,30,35−37] eventually assigning (i) the very low quantum yield at room temperature to the existence of low-lying ligand-to-metal charge transfer (LMCT) excited states[36] and (ii) the large red-shift of the $Eu(^5D_0 \leftarrow ^7F_0)$ transition to an exceptionally large nephelauxetic effect produced by heterocyclic nitrogen donor atoms, $\delta_{N\text{-het}} = -15.8(9)$ cm^{-1} in eq 3,[37] whereby C_{CN} is an empirical coefficient depending upon the Eu(III) coordination number, with $C_{CN} = 1$ for nine-coordinated complexes, n_i is the number of coordinated atom of type i, $\tilde{\nu}_0 = 17\,374$ cm^{-1} at 295 K is the energy of the $Eu(^5D_0 \leftarrow ^7F_0)$ transition in the free ion, and δ_i is the nephelauxetic parameter of the donor atom i.[38]

$$\tilde{\nu} = \tilde{\nu}_0 + C_{CN} \sum_i n_i \cdot \delta_i \quad (3)$$

This nephelauxetic parameter was determined as follows. The low quantum yield of the EuN_9 site usually restricts the detection of the $Eu(^5D_0 \leftarrow ^7F_0)$ transition at low temperatures, at which nonradiative quenching processes are limited. The energy of the transition was found to be 17 223 cm^{-1} for $[Eu(\mathbf{L10})_3]^{3+}$ at 77 K,[30] 17 219 cm^{-1} for $[Eu(\mathbf{L12})_3]^{3+}$ at 77 K,[29] and 17 224 cm^{-1} for the noncovalent podate *HHH*-$[EuZn(\mathbf{L13})_3]^{5+}$ at 10 K, each complex possessing the same EuN_9 site (Charts 2 and 3).[37] These values were then translated at 295 K into $\tilde{\nu} = 17\,232$, 17 228, and 17 236 cm^{-1}, respectively, by using the accepted temperature

(35) Petoud, S.; Bünzli, J.-C. G.; Schenk, K. J.; Piguet, C. *Inorg. Chem.* **1997**, *36*, 1345–1353.
(36) Petoud, S.; Bünzli, J.-C. G.; Piguet, C.; Xiang, Q.; Thummel, R. *J. Lumin.* **1999**, *82*, 69–79.
(37) Piguet, C.; Rivara-Minten, E.; Hopfgartner, G.; Bünzli, J.-C. G. *Helv. Chim. Acta* **1995**, *78*, 1541–1566.
(38) Frey, S. T.; Horrocks, W. deW., Jr. *Inorg. Chim. Acta* **1995**, *229*, 383–390.

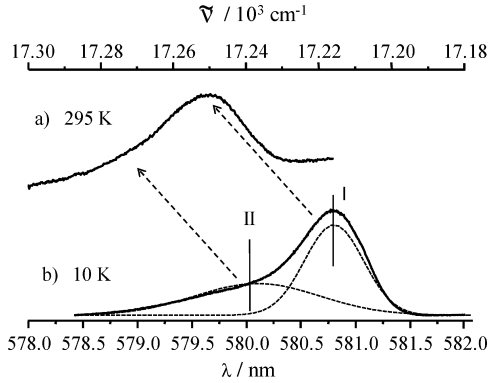

Figure 3. Laser-induced high-resolution excitation spectra of the $^5D_0 \leftarrow {}^7F_0$ transition in $[Eu(\mathbf{L9})]^{3+}$ recorded in the solid state at (a) 295 K and (b) 10 K.

dependence of 1 cm^{-1}/24 K.[39] Subsequent application of eq 3 led to $\delta_{N\text{-het}} = -15.8(9)$ cm^{-1}.

In the more constrained polynuclear triple-stranded helicates $[Eu_3(\mathbf{L14})_3]^{9+}$ [40] and $[Eu_4(\mathbf{L15})_3]^{12+}$ (Chart 3), [41] the energies of the Eu($^5D_0 \leftarrow {}^7F_0$) transitions of the central EuN_9 sites at 10 K amounted to 17 238 and 17 235 cm^{-1}, respectively. The translation at 295 K gave a reduced nephelauxetic parameter of $\delta_{N\text{-heterocyclic}} = -13.7$ cm^{-1}, a value closer to $\delta_N = -12.1$ cm^{-1} estimated for amine donor groups,[38] which was tentatively assigned to geometrical and electronic constraints arising from the capping EuN_6O_3 sites in these extended polynuclear helicates.[41] Interestingly, the emission spectra of the podate $[Eu(\mathbf{L9})]^{3+}$ shed new light on this problem, because they are intense enough for safely recording the laser-induced high-resolution excitation spectra of the Eu($^5D_0 \leftarrow {}^7F_0$) transition for the EuN_9 site at both 295 and 10 K (Figure 3).

We observe a major site (I) flanked with a minor shoulder at higher energy (site II) at both temperatures. At 295 K, the main broad band is centered at 17 252 cm^{-1} (site I, Figure 3a), from which a nephelauxetic parameter $\delta_{N\text{-het}} = -13.6$ cm^{-1} is calculated with eq 3 for $[Eu(\mathbf{L9})]^{3+}$, in agreement with the value extrapolated from a multisite analysis of polynuclear triple-stranded helicates.[39,40] At 10 K, the major site is observed at 17 218 cm^{-1} (Figure 3b), thus pointing to a quite large and unusual 1.2 cm^{-1}/10 K dependence of the energy of the Eu($^5D_0 \leftarrow {}^7F_0$) transition on the temperature. This result explains the inconsistency in the data previously extrapolated from low-temperature excitation spectra, and its origin can be tentatively attributed to the existence of the low-lying LMCT states associated with this EuN_9 site, whose variable energetic location in the different complexes may perturb the behavior of intrashell Eu($^5D_0 \leftarrow {}^7F_0$) transition.

Selective excitation of the major site I of $[Eu(\mathbf{L9})]^{3+}$ ($\tilde{\nu}_{exc}$ = 17 218 cm^{-1} at 10 K, Figure 4b) produces an emission spectrum very similar to that obtained upon broadband

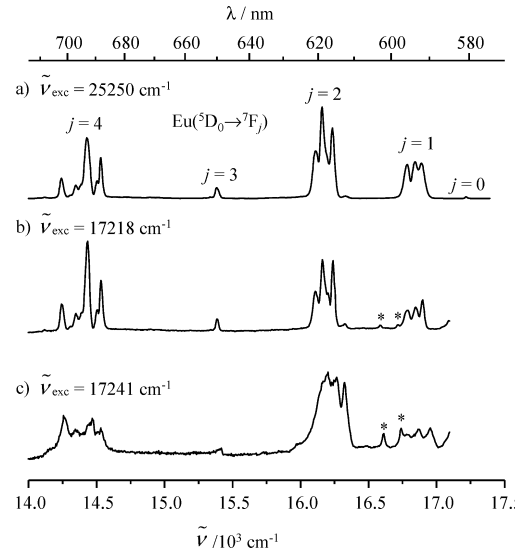

Figure 4. High-resolution emission spectra obtained for $[Eu(\mathbf{L9})]^{3+}$ at 10 K in the solid state upon irradiation of (a) ligand-centered $\pi\pi^*$ levels, (b) Eu($^5D_0 \leftarrow {}^7F_0$) in site I, and (c) Eu($^5D_0 \leftarrow {}^7F_0$) in site II (* = artifacts).

excitation of the ligand-centered $\pi\pi^*$ levels (Figure 4a). The splitting pattern is diagnostic for a EuN_9 site in a low-symmetrical environment. The observation of three regularly spaced components for the Eu($^5D_0 \rightarrow {}^7F_1$) transition unambiguously demonstrates the lack of 3-fold symmetry (Figure 4; Table S4, Supporting Information), for which only two components (A + E) are expected (and indeed observed in $[Eu(\mathbf{L10})_3]^{3+}$).[30] The detection of respectively four components for the hypersensitive electric dipolar transition $^5D_0 \rightarrow {}^7F_2$, while only three are predicted in C_3-symmetry (A + 2E), confirms the low symmetry of the europium site. Selective excitation of the minor site II ($\tilde{\nu}_{exc}$ = 17 241 cm^{-1} at 10 K, Figure 4c) produces a very weak emission spectrum (5.5% of the total intensity obtained upon ligand irradiation), whose crystal-field splitting is reminiscent of that discussed for site I. Finally, direct excitation of the $^5D_0 \leftarrow {}^7F_0$ transition of $[Eu(\mathbf{L9})]^{3+}$ at 10 K results in a biexponential emission decay with characteristic Eu($^5D_0$) lifetimes of 1.63(5) (89%) and 0.07 ms (11%), reasonably assigned as arising from sites I and II, respectively. Compared with $\tau_{Eu(5D0)}$ = 1.85(4) ms obtained for $[Eu(\mathbf{L10})_3]^{3+}$ (77 K)[30] and $\tau_{Eu(5D0)}$ = 1.66−1.75 ms for $[Eu(\mathbf{L12})_3]^{3+}$ (77 K),[29] the lifetime of the major EuN_9 site in $[Eu(\mathbf{L9})]^{3+}$ proves the absence of high-energy oscillators in the first coordination sphere.

Solution Behavior and Assignment of ^{1}H NMR Paramagnetic Spectra. The ^{1}H NMR spectra of the diamagnetic complexes $[La(\mathbf{L9})]^{3+}$, $[Lu(\mathbf{L9})]^{3+}$, and $[Y(\mathbf{L9})]^{3+}$ in CD_3CN display 23 well-resolved signals, which are diagnostic for the formation of rigid C_3-symmetrical podates (i.e., three equivalent tridentate binding units) on the NMR time scale at room temperature (Figure 5a; Table S5, Supporting Information). The three signals with triple intensity correspond to the methyl groups bound to the benzimidazole rings (H15, H17, and H18, numbering in Chart 2 and Figure 5). The 20 remaining signals can be assigned to the capping methyl group (H1), together with nine aromatic protons (H5−H13) and 10 diastereotopic methylene groups (H2−H4, H14, and H16) by using two-dimensional {^{1}H−^{1}H} correla-

(39) Bünzli, J.-C. G. In *Lanthanide Probes in Life, Chemical and Earth Sciences*; Bènzli, J.-C., G., Choppin, G. R., Eds.; Elsevier: Amsterdam, 1989; Chapter 7.
(40) Floquet, S.; Ouali, N.; Bocquet, B.; Bernardinelli, G.; Imbert, D.; Bünzli, J.-C. G.; Hopfgartner, G.; Piguet, C. *Chem. Eur. J.* **2003**, *9*, 1860–1875.
(41) Dalla Favera, N.; Hamacek, J.; Borkovec, M.; Jeannerat, D.; Gumy, F.; Bünzli, J.-C. G.; Ercolani, G.; Piguet, C. *Chem.—Eur. J.* **2008**, *14*, 2994–3005.

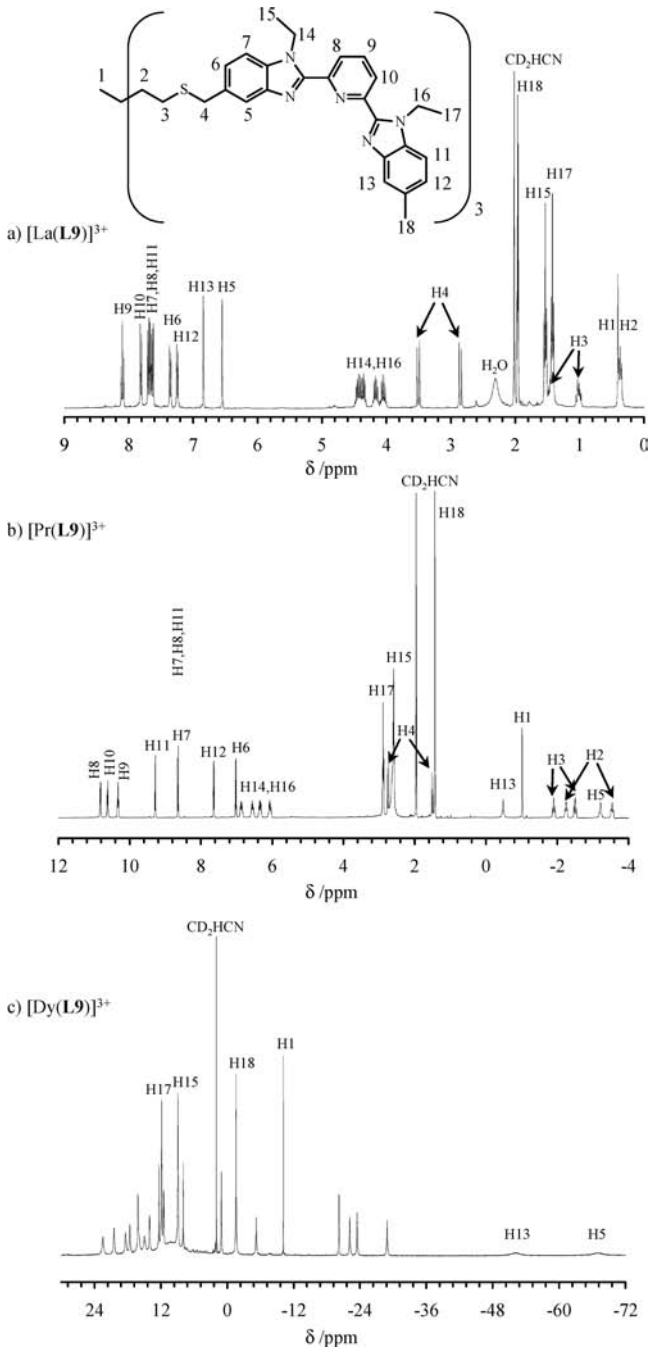

Figure 5. ^{1}H NMR spectra of (a) [La(**L9**)]$^{3+}$, (b) [Pr(**L9**)]$^{3+}$, and (c) [Dy(**L9**)]$^{3+}$ (CD_3CN, 298 K).

tion spectroscopy (COSY) and {^{1}H−^{1}H} nuclear Overhauser effect spectrometry (NOESY) spectra. Interestingly, the observation of strong NOE effects within the H8−H14 and H10−H16 pairs implies cis−cis conformations for the tridentate binding units resulting from their meridional coordination to Ln(III). Except for some additional paramagnetic contributions (i) to the chemical shifts (lanthanide-induced shift) and (ii) to the nuclear relaxation (lanthanide-induced relaxation, LIR), the replacement of the diamagnetic lanthanides with their paramagnetic counterparts in the first half of the series (Ln = Ce−Eu, except Pm) does not bring special difficulty in the assignment of the 23 signals by using through-bond (COSY) and through-space (NOESY) correlation NMR spectra (Figure 5b; Table S5, Supporting Information).

The additional contribution to the longitudinal nuclear relaxation (LIR) brought by the electron spin of fast relaxing paramagnetic lanthanides (eq 4, Ln = Ce−Yb, except Gd) is largely dominated by transient and static (i.e., Curie spin) dipolar electron−nucleus interactions modeled with eq 5 (μ_0 is the permittivity of the vacuum, γ_I is the gyromagnetic ratio of the nucleus, μ^{eff} is the effective electronic magnetic moment, β is the Bohr magneton, τ_e is the electronic correlation time, H_0 is the applied magnetic field, r_i is the Ln−nucleus distance, T is the temperature, k is Boltzmann's constant, τ_r is the rotational correlation time, and ω_I is the Larmor frequency of the nucleus).[42−46]

$$1/T_{1i}^{\text{para}} = 1/T_{1i}^{\text{exp}} - 1/T_{1i}^{\text{dia}} \quad (4)$$

$$\frac{1}{T_{1i}^{\text{para}}} = \frac{1}{T_{1i}^{\text{transcient}}} + \frac{1}{T_{1i}^{\text{static}}} = \frac{4}{3}\left(\frac{\mu_0}{4\pi}\right)^2 \frac{\gamma_I \mu_{\text{eff}}^2 \beta^2}{r_i^6}\tau_e + \frac{6}{5}\left(\frac{\mu_0}{4\pi}\right)^2 \frac{\gamma_I^2 \mu_{\text{eff}}^4 \beta^4 H_0^2}{r_i^6 (3kT)^2}\left(\frac{\tau_r}{1+\omega_I^2\tau_r^2}\right) = E_j\left(\frac{1}{r_i^6}\right) \quad (5)$$

Since both transient and static dipolar contributions depend on r_i^{-6} for a given complex at a fixed temperature, we expect a linear correlation between $1/T_{1i}^{\text{para}}$ and r_i^{-6} for all protons in each [Ln(**L9**)]$^{3+}$ complex (slope E_j in eq 5). The C_3-averaged $r_{\text{Eu-H}i}$ distances have been taken from the crystal structure of [Eu(**L9**)]$(ClO_4)_4$[27] and used without correction of the CH distances for the solution structure[47] (Table S7, Supporting Information). Plots of $1/T_{1i}^{\text{para}}$ (obtained by using eq 4 with T_{1i}^{exp} and T_{1i}^{dia} collected in Table S6, Supporting Information) versus r_i^{-6} for protons H1, H5, H13, H15, H17, and H18 in [Ln(**L9**)]$^{3+}$ (Ln = Ce−Eu, Figure 6a) indeed lead to satisfying straight lines, which indicates (i) a correct assignment for these protons and (ii) that the crystal structure of [Eu(**L9**)]$(ClO_4)_3$ is, at first sight, an acceptable model for the averaged structure adopted by [Ln(**L9**)]$^{3+}$ in solution. The attribution of the ^{1}H NMR spectra recorded for the complexes [Ln(**L9**)]$^{3+}$ of the second part of the lanthanide series (Ln = Tb−Yb) is complicated by the larger electronic magnetic moments (influence of μ^{eff} in eq 5), which increases $1/T_{1i}^{\text{para}}$ and $1/T_{2i}^{\text{para}}$ to such an extent that scalar and dipolar couplings cannot be reliably detected (Figure 5c). Among the 23 broad and overlapping signals, the two protons, H5 and H13, located closest to the paramagnetic center are easily recognized because of their considerable pseudo-contact shifts (see next section), which move them into a spectral

(42) Peters, J. A.; Huskens, J.; Raber, D. J. *Prog. Nucl. Magn. Reson. Spectrosc.* **1996**, *28*, 283–350.
(43) Forsberg, J. H. In *Handbook on the Physics and Chemistry of Rare Earths*; Gschneidner, K. A., Jr., Eyring, L., Eds.; Elsevier: Amsterdam, 1996; Vol. 23, Chapter 153, pp 1−68.
(44) Piguet, C.; Geraldes, C. F. G. C. In *Handbook on the Physics and Chemistry of Rare Earths*; Gschneidner, K. A., Jr., Bünzli, J.-C. G., Pecharsky, V. K., Eds.; Elsevier Science: Amsterdam, 2003; Vol. 33, Chapter 215, pp 353−463.
(45) Bertini, I.; Luchinat, C.; Parigi, G. *Prog. Nucl. Magn. Reson. Spectrosc.* **2002**, *40*, 249–273.
(46) Bertini, I.; Luchinat, C. *Coord. Chem. Rev.* **1996**, *150*, 1–292.
(47) Henry, B. R. *Acc. Chem. Res.* **1987**, *20*, 429–435.

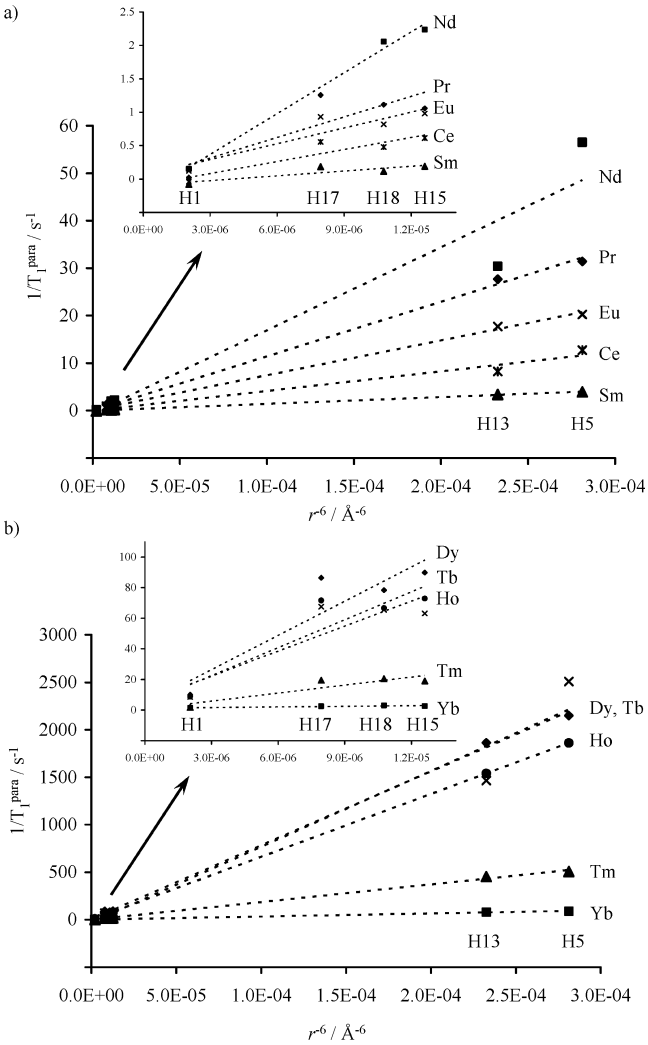

Figure 6. Plots of $1/T_{1i}^{para}$ versus r_i^{-6} according to eq 5 for H1, H5, H13, H15, H17, and H18 for (a) Ln = Ce−Eu and (b) Ln = Dy−Yb (CD_3CN, 298 K).

Table 1. ^{1}H NMR Chemical Shifts (δ^{exp} /ppm *vs* TMS) for Protons H1, H5, H13, H15, H17, and H18 in $[Ln(\mathbf{L9})]^{3+}$ (CD_3CN, 298 K)[a]

compd	H1	H5	H13	H15	H17	H18
$[La(\mathbf{L9})]^{3+}$	0.39	6.52	6.81	1.51	1.40	1.99
$[Y(\mathbf{L9})]^{3+}$	0.40	6.35	6.52	1.48	1.48	1.92
$[Lu(\mathbf{L9})]^{3+}$	0.41	6.29	6.42	1.50	1.50	1.91
$[Ce(\mathbf{L9})]^{3+}$	−0.23	3.46	1.98	2.00	2.10	1.73
$[Pr(\mathbf{L9})]^{3+}$	−1.04	−3.24	−0.51	2.57	2.56	1.41
$[Nd(\mathbf{L9})]^{3+}$	−0.48	2.23	0.65	2.15	2.32	1.56
$[Sm(\mathbf{L9})]^{3+}$	0.26	5.42	5.85	1.60	1.60	1.90
$[Eu(\mathbf{L9})]^{3+}$	1.23	11.58	10.75	0.90	0.68	2.42
$[Tb(\mathbf{L9})]^{3+}$	−6.53	−35.35	−46.79	6.85	9.26	−0.32
$[Dy(\mathbf{L9})]^{3+}$	−10.11	−66.00	−52.00	9.01	11.93	−1.63
$[Ho(\mathbf{L9})]^{3+}$	−7.17	−48.46	−38.43	6.83	8.64	−1.13
$[Tm(\mathbf{L9})]^{3+}$	3.46	26.98	24.14	−0.82	−2.28	3.05
$[Yb(\mathbf{L9})]^{3+}$	2.20	17.57	15.99	0.25	−0.37	2.55

[a] See Chart 2 for the atom-numbering scheme.

domain remote from the other signals (Figure 5c and Table 1).

Signals from the three methyl groups H15, H17, and H18 are also easily assigned because of their triple intensities, and H1 is sufficiently separated from the paramagnetic center to minimize LIR effects, thus giving a single sharp singlet with an integral of 1.0 (Figure 5b,c). Once these signals have been located in the spectra of the strongly paramagnetic complexes $[Ln(\mathbf{L9})]^{3+}$ (Ln = Tb−Yb), systematic permutations of the peaks lead to a unique satisfying straight line according to eq 5, thus leading to the definitive assignment of the chemical shifts for these protons collected in Table 1. Please note that, for Ln = Er, a drastic overlap of broad signals prevents a definitive and safe assignment of the methyl protons, and this complex was not included in further analysis.

Isostructurality, Solution Structure, and Molecular Paramagnetic Tensors. The experimental NMR hyperfine shift of a nucleus *i* in a paramagnetic complex of a lanthanide *j* (δ_{ij}^{exp} in ppm) can be partitioned according to eq 6, whereby δ_i^{dia} contains the underlying diamagnetic shift measured for the analogous $4f^0$ (Ln = La, Y) or $4f^{14}$ (Ln = Lu) electronic configurations, and δ_j^{bulk} is the bulk paramagnetic susceptibility of the solution ($\delta_j^{bulk} = 0$ when an internal reference is used).[42–44]

$$\delta_{ij}^{exp} = \delta_i^{dia} + \delta_j^{bulk} + \delta_{ij}^{para} \quad (6)$$

The hyperfine paramagnetic contribution δ_{ij}^{para} is thus easily obtained from the experimental data (eq 7; Table S8, Supporting Information), and it corresponds to the sum of the contact (through-bond, δ_{ij}^{c}, eq 8) and pseudo-contact (through-space, δ_{ij}^{pc}, eq 9) effects brought by the electronic magnetic momentum.[42–46]

$$\delta_{ij}^{para} = \delta_{ij}^{exp} - \delta_i^{dia} = \delta_{ij}^{c} + \delta_{ij}^{pc} \quad (7)$$

$$\delta_{ij}^{c} = \frac{A_i}{\hbar\gamma_i H^0}\langle S_z\rangle_j = F_i\langle S_z\rangle_j \quad (8)$$

$$\delta_{ij}^{pc} = \frac{1}{2N_A r_i^3}\left[\left(\chi_{zz}^j - \frac{1}{3}\mathrm{Tr}\chi^j\right)(3\cos^2\theta_i - 1) + (\chi_{xx}^j - \chi_{yy}^j)(\sin^2\theta_i \cos 2\varphi_i)\right] \quad (9)$$

The contact contribution δ_{ij}^{c} results from the delocalization of the electronic spin brought by the paramagnetic lanthanide *j* onto the nucleus *i*, which is mediated by scalar Fermi interactions.[48,49] It thus reflects the topology and the nature of the chemical bonds separating the metal from the nucleus under investigation. Since the covalency of Ln−ligand bonds is minute, the Fermi hyperfine constants A_i are small (and consequently F_i are small in eq 8), which limits the delocalization of unpaired spin over three, or at most four, bonds remote from the metallic center. $\langle S_z\rangle_j$ is the thermally averaged spin expectation value of the lanthanide *j*, for which data tabulated for the free ions at 300 K are satisfying approximations for coordination complexes in solution.[48] The pseudo-contact contribution δ_{ij}^{pc} results from the dipolar coupling between the electronic and magnetic momenta, which depends on (i) the magnitude of the paramagnetic anisotropy induced by the lanthanide metal ion (via $\chi_{zz}^j - 1/3\mathrm{Tr}\chi^j$ and $\chi_{xx}^j - \chi_{yy}^j$ in eq 9, whereby χ_{xx}^j, χ_{yy}^j, and χ_{zz}^j are the components of the molecular paramagnetic susceptibility tensor in the principal magnetic axes system) and (ii) the

(48) Golding, R. M.; Halton, M. P. *Aust. J. Chem.* **1972**, *25*, 2577–2581.
(49) Pinkerton, A. A.; Rossier, M.; Spiliadis, S. *J. Magn. Reson.* **1985**, *64*, 420–425.

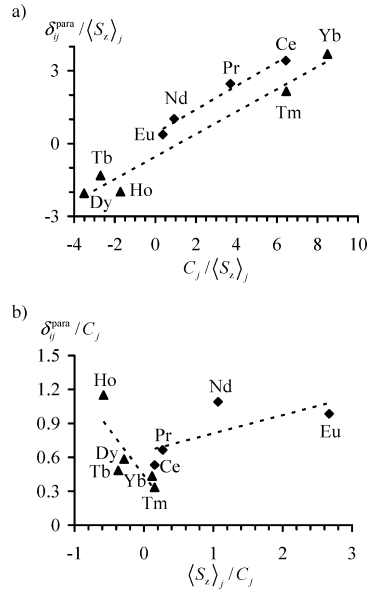

Figure 7. Plots of (a) $\delta_{ij}^{para}/\langle S_z\rangle_j$ versus $C_j/\langle S_z\rangle_j$ and (b) δ_{ij}^{para}/C_j versus $\langle S_z\rangle_j/C_j$ for protons H13 in $[Ln(\mathbf{L9})]^{3+}$ (CD_3CN, 298 K, Ln = Ce−Yb, except Pm, Gd and Er; Sm is not shown because of its faint paramagnetism).

geometrical position of the nucleus within the molecular architecture (via the polar coordinates r_i, θ_i, and ϕ_i of the nucleus i in the principal magnetic axes system; N_A is Avogadro's number).[42,43] The pseudo-contact shift δ_{ij}^{pc} thus contains the structural information of interest. Assuming a weak effect of the donor atom on the splitting of the lanthanide ground-state multiplet at room temperature ($kT > \Delta E_{CF}$, whereby ΔE_{CF} is the crystal-field splitting), Bleaney proposed a high-temperature expansion of the paramagnetic suceptibility tensor in a power series in the inverse of the temperature T^{-n}, and limited to $n = 2$.[50] While the resulting Curie term ($n = 1$) corresponds to the isotropic part of the tensor ($\chi_0 = 1/3\mathrm{Tr}(\chi^j)$), which has thus no effect on δ_{ij}^{pc}, the second term in T^{-2} (eqs 10 and 11) is a satisfying approximation for the anisotropic part of the paramagnetic susceptibility tensor, whereby B_q^2 ($q = 0, 2$) are the conventional second-rank crystal-field parameters,[51,52] ξ^j is a numerical coefficient tabulated for each $4f^n$ configuration,[50] $(1 + p^j)$ reflects the contribution of thermally populated excited multiplets of the lanthanide ion, and β is the Bohr magneton. The common numerical term $C_j = -\beta^2(1 + p^j)\xi^j/60(kT)^2$, often referred to as Bleaney's factor, can be calculated for each lanthanide j at 300 K, and its relative value, scaled to $C_{Dy} = -100$, has been tabulated (entry 5, Table 4).[44,50]

$$\chi_{zz}^j - \frac{1}{3}\mathrm{Tr}(\chi^j) = -\frac{N_A\beta^2(1+p^j)\xi^j}{60(kT)^2}2B_0^2 = 2N_AC_jB_0^2 \quad (10)$$

$$\chi_{xx}^j - \chi_{yy}^j = -\frac{N_A\beta^2(1+p^j)\xi^j}{60(kT)^2}2\sqrt{6}B_2^2 = 2N_AC_j\sqrt{6}B_2^2 \quad (11)$$

Introducing eqs 10 and 11 into eq 9 yields

$$\delta_{ij}^{pc} = C_j\left[B_0^2\left(\frac{3\cos^2\theta_i - 1}{r_i^3}\right) + \sqrt{6}B_2^2\left(\frac{\sin^2\theta_i\cos 2\varphi_i}{r_i^3}\right)\right] \quad (12)$$

Since $[Ln(\mathbf{L9})]^{3+}$ podates possess a 3-fold axis in solution on the NMR time scale along the complete lanthanide series, the paramagnetic tensor is axial (i.e., $B_2^2 = 0$), and eq 12 reduces to eq 13, whereby the term $G_i = (3\cos^2\theta_i - 1)/r_i^3$ is known as the geometrical factor.

$$\delta_{ij}^{pc} = B_0^2 \cdot G_i \cdot C_j \quad (13)$$

Introducing eqs 8 and 13 into eq 7 eventually yields eq 14, from which two straightforward linear forms (eqs 15 and 16) can be used for unraveling isostructurality along the lanthanide series.[42–44]

$$\delta_{ij}^{para} = F_i\langle S_z\rangle_j + B_0^2G_iC_j \quad (14)$$

$$\delta_{ij}^{para}/\langle S_z\rangle_j = F_i + B_0^2G_i(C_j/\langle S_z\rangle_j) \quad (15)$$

$$\delta_{ij}^{para}/C_j = B_0^2G_i + F_i(\langle S_z\rangle_j/C_j) \quad (16)$$

Plots of $\delta_{ij}^{para}/\langle S_z\rangle_j$ versus $C_j/\langle S_z\rangle_j$ (eq 15) or δ_{ij}^{para}/C_j versus $\langle S_z\rangle_j/C_j$ (eq 16) for protons H1, H5, H13, H15, H17, and H18 show that two different straight lines, one for the light (Ln = Ce−Eu) and one for the heavy paramagnetic lanthanides (Ln = Dy−Yb), are required for satisfyingly fitting the data (Figure 7 and Figure S1−S5, Supporting Information; δ_{ij}^{para} are taken from Table S8). Multilinear least-squares fits of eq 14 for every proton along the two half-lanthanide series give two sets of F_i and $B_0^2G_i$ parameters (Table 2). The paramagnetic chemical shifts $\delta_{ij}^{para,calcd}$ computed from these parameters (Table S9, Supporting Information) fairly match the experimental values with agreement factors $0.21 < AF_i < 0.48$ (eq 17),[53] in line with those previously reported for triple-helical complexes $[Ln(\mathbf{L10})_3]^{3+}$,[28] and for related trigonal lanthanide complexes with tridentate ligands.[44]

$$AF_i = \sqrt{\frac{\sum_{j=Ce}^{Yb}(\delta_{ij}^{para,\,exp} - \delta_{ij}^{para,\,calcd})^2}{\sum_{j=Ce}^{Yb}(\delta_{ij}^{para,\,exp})^2}} \quad (17)$$

The break between the two linear series, often referred to as the gadolinium break,[54] has a long history[44] and usually originates from the regular contraction of the 4f orbitals, which stepwise decreases B_0^2.[44] This variation is amplified for the $4f^{8-13}$ electronic configurations (Ln = Tb−Yb) because of their large paramagnetic anisotropies; that is, the Bleaney factors abruptly vary from $-11 \le C_j \le +4$ for Ln = Ce−Eu to $-100 \le C_j \le +53$ for Ln = Tb−Yb, while

(50) Bleaney, B. *J. Magn. Reson.* **1972**, *8*, 91–100.
(51) Mironov, V. S.; Galyametdinov, Y. G.; Ceulemans, A.; Görller-Walrand, C.; Binnemans, K. *Chem. Phys. Lett.* **2001**, *345*, 132–140.
(52) Mironov, V. S.; Galyametdinov, Y. G.; Ceulemans, A.; Görller-Walrand, C.; Binnemans, K. *J. Chem. Phys.* **2002**, *116*, 4673–4685.
(53) Willcott, M. R.; Lenkinski, R. E.; Davis, R. E. *J. Am. Chem. Soc.* **1972**, *94*, 1742–1744.
(54) Rigault, S.; Piguet, C. *J. Am. Chem. Soc.* **2000**, *122*, 9304–9305.

Table 2. Computed Values for Contact (F_i), Pseudo-Contact ($B_0^2G_i$) Terms, and Agreement Factors (AF_i) for ^1H Nuclei in the Podates $[Ln(\mathbf{L9})]^{3+}$ (Ln = Ce−Yb, CD_3CN, 298 K)[a]

compd		H1	H5	H13	H15	H17	H18
Ln = Ce−Eu	F_i	0.04(2)	0.2(1)	0.2(2)	−0.03(1)	−0.04(2)	0.03(1)
	$B_0^2G_i$	0.11(2)	0.7(1)	0.7(2)	−0.09(1)	−0.10(2)	0.05(1)
	AF_i	0.37	0.39	0.33	0.35	0.30	0.48
Ln = Tb−Yb	F_i	−0.11(7)	−0.7(6)	−0.8(3)	0.07(4)	0.09(6)	−0.04(3)
	$B_0^2G_i$	0.07(2)	0.4(2)	0.4(1)	−0.05(1)	−0.08(2)	0.02(1)
	AF_i	0.28	0.32	0.22	0.25	0.21	0.36

[a] See Chart 2 for the atom-numbering scheme.

Table 3. Computed Values for $(F_i-F_k(G_i/G_k))$ and G_i/G_k Parameters Obtained in Solution with eq 18 for Hi−Hk Pairs in $[Ln(\mathbf{L9})]^{3+}$ (Ln = Ce−Yb, except Pm, Gd and Er, CD_3CN, 298 K), and G_i/G_k Parameters Calculated with eq 19 in the Solid State for the Crystal Structure of $[Eu(\mathbf{L9})](ClO_4)_3$

	H1−H5	H1−H13	H1−H15	H1−H17	H1−H18	H5−H13	H5−H15	H5−H17
R^2 [a]	0.987	0.990	0.999	0.980	0.962	0.984	0.980	0.993
$F_i-F_k(G_i/G_k)$	0.06(3)	0.03(3)	−0.015(9)	0.05(4)	0.07(5)	−0.2(3)	−0.6(3)	−0.0(2)
G_i/G_k solution	0.126(5)	0.140(5)	−1.42(2)	−0.70(4)	1.6(1)	1.10(5)	−11.1(6)	−5.5(2)
G_i/G_k solid[b]	0.176	0.286	−1.537	−1.812	6.985	1.624	−8.718	−10.278
G_i/G_k solid A[c]	0.157	0.184	−6.386	−1.848	1.851	1.174	−40744	−11.790
G_i/G_k solid B[c]	0.182	−1.471	−3.055	−1.231	−1.701	−8.077	−16.772	−6.755
G_i/G_k solid C[c]	0.194	0.175	−0.681	−3.309	2.096	0.899	−3.508	−17.044

	H5−H18	H13−H15	H13−H17	H13−H18	H15−H17	H15−H18	H17−H18
R^2	0.988	0.989	0.991	0.979	0.974	0.953	0.994
$F_i-F_k(G_i/G_k)$	0.0(2)	−0.3(2)	0.2(2)	0.3(3)	−0.05(3)	−0.06(4)	−0.02(3)
G_i/G_k solution	12.6(5)	−10.0(4)	−5.0(2)	11.3(6)	0.49(3)	−1.11(8)	−2.27(6)
G_i/G_k solid [b]	39.631	−5.369	−6.330	24.408	1.179	−4.546	−3.856
G_i/G_k solid A[c]	11.812	−34.699	−10.041	10.060	0.289	−0.290	−1.002
G_i/G_k solid B[c]	−9.339	2.077	0.836	1.156	0.403	0.557	1.382
G_i/G_k solid C[c]	10.796	−3.901	−18.955	12.006	4.859	−3.078	−0.633

[a] Correlation coefficient for the linear dependence of $\delta_{ij}^{para}/\langle S_z\rangle_j$ versus $\delta_{kj}^{para}/\langle S_z\rangle_j$ plots. [b] Obtained for the C_3-averaged crystal structure. [c] A, B, and C refer to strands A, B, and C, respectively.

Table 4. Anisotropic Part of the Axial Molecular Paramagnetic Susceptibility Tensor ($\Delta\chi^j = \chi^j_{zz} - \chi^j_{xx}$ in $cm^3\cdot mol^{-1}$) and Contact Shifts (δ^c_{H5} and δ^c_{H13} in ppm) Obtained for $[Ln(\mathbf{L9})]^{3+}$ in CD_3CN by Using Multilinear Least-Squares Fits of eqs 20 and 21 (Ln = Ce−Yb, except Pm, Gd and Er)

	Ce	Pr	Nd	Sm	Eu	Tb	Dy	Ho	Tm	Yb
$\Delta\chi^j \times 10^3$ (eq 20)	−0.42(5)	−0.90(6)	−0.49(6)	−0.118(6)	0.26(2)	−2.7(3)	−5.0(4)	−3.7(3)	2.9(1)	1.40(6)
$\Delta\chi^j \times 10^3$ (eq 21)	−0.4(1)	−0.9(1)	−0.6(1)	−0.1(4)	0.5(1)	−5(1)	−7(2)	−5(1)	2.1(6)	1.1(3)
δ^c_{H5}	1(1)	−2(1)	0(1)	−0.2(3)	0.2(9)	−0(12)	−13(15)	−12(10)	2(6)	1(3)
δ^c_{H13}	−1(1)	0(1)	−1(1)	−0.1(3)	−0.7(9)	−13(11)	−0(15)	−3(10)	−0(6)	−0(3)
C_j[a]	−6.3	−11	−4.2	−0.7	4.0	−86.0	−100.0	−39.0	53.0	22.0

[a] Bleaney's factors taken from ref 44.

$C_{Gd} = 0$.[44,50] In some rare cases,[44] this phenomenon is combined with important structural changes, which affect G_i along the lanthanide series, thus producing additional breaks in the linear correlations described in eqs 15 and 16.[44] In order to remove the underlying crystal-field effect and to decide whether isostructurality is a characteristics of the $[Ln(\mathbf{L9})]^{3+}$ podates along the series, we have resorted to the crystal-field-independent eq 18, in which the second-rank crystal-field parameters are removed by a judicious combination of two equations identical to eq 14, but referring to two different protons i and k in the same complex.[44,55,56]

$$\frac{\delta_{ij}^{para}}{\langle S_z\rangle_j} = \left(F_i - F_k\cdot\frac{G_i}{G_k}\right) + \frac{G_i}{G_k}\cdot\frac{\delta_{kj}^{para}}{\langle S_z\rangle_j} \qquad (18)$$

Plots of $\delta_{ij}^{para}/\langle S_z\rangle_j$ versus $\delta_{kj}^{para}/\langle S_z\rangle_j$ (eq 18) along the complete lanthanide series for each possible pair of protons (i,j = H1, H5, H13, H15, H17, and H18) are strictly linear (Figure 8 and Table 3). We can thus safely conclude that the geometrical factors G_i do not vary along the series and that the $[Ln(\mathbf{L9})]^{3+}$ podates adopt a single averaged C_3-symmetrical structure in solution for Ln = Ce−Yb. Consequently, we can deduce the ratio B_0^2 (Ln = Ce−Eu)/B_0^2 (Ln = Tb−Yb) = 1.6(6) from Table 2, a value in complete agreement with similar data reported for $[Ln(\mathbf{L10})_3]^{3+}$ and for related tridentate ligands.[44] Moreover, the ratios of the geometrical factors G_i/G_k obtained for $[Ln(\mathbf{L9})]^{3+}$ in solution (eq 18, Table 3) can be compared with those calculated from the crystal structure of $[Eu(\mathbf{L9})](ClO_4)_3$ by using eq 19, whereby θ_i and r_i are the polar coordinates in the principal magnetic axes system (i.e., the Eu(III) atom lies at the origin, and the z axis coincides with the pseudo-C_3 axis passing through Eu(III) and the apical quaternary carbon atom, see Figure 2c and Table S7).

$$\frac{G_i}{G_k} = \left(\frac{3\cos^2\theta_i - 1}{3\cos^2\theta_k - 1}\right)\cdot\left(\frac{r_k}{r_i}\right)^3 \qquad (19)$$

Since the ethyl groups bearing protons H15 and H17 are too flexible for being used as structural probes for comparing solid state and solution structures, we limit the comparison to the six Hi−Hk pairs involving protons H1, H5, H13, and H18

(55) Spiliadis, S.; Pinkerton, A. A. *J. Chem. Soc., Dalton Trans.* **1982**, 1815–1818.
(56) Platas, C.; Avecilla, F.; de Blas, A.; Geraldes, C. F. G. C.; Rodriguez-Blas, T.; Adams, H.; Mahia, J. *Inorg. Chem.* **1999**, *38*, 3190–3199.

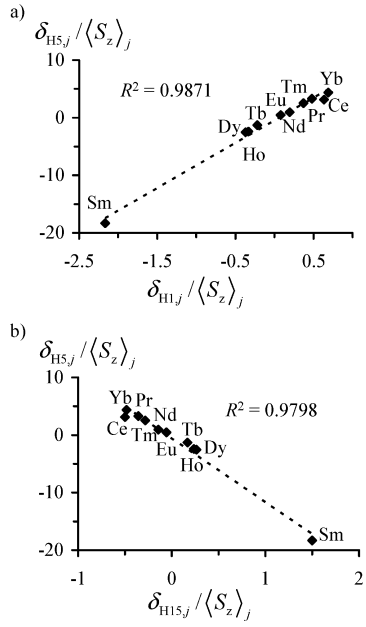

Figure 8. Plots of $\delta_{ij}^{para}/\langle S_z\rangle_j$ versus $\delta_{kj}^{para}/\langle S_z\rangle_j$ for (a) H1−H5 and (b) H15−H5 proton pairs in $[Ln(\mathbf{L9})]^{3+}$ (CD_3CN, 298 K, Ln = Ce−Yb, except Pm, Gd and Er).

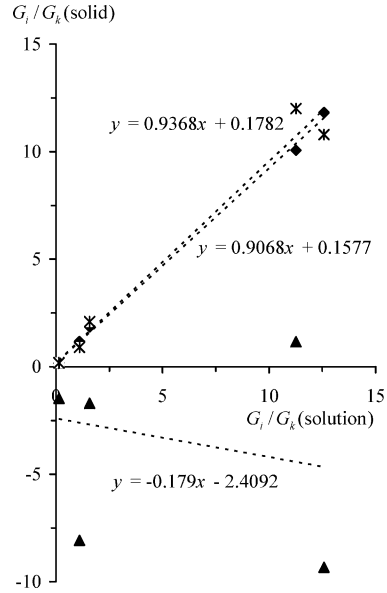

Figure 9. Correlations between G_i/G_k for six Hi−Hk pairs involving protons H1, H5, H13, and H18, obtained at 298 K in CD_3CN solution (eq 18) and in the solid state (eq 19) for strands A (rhombs), B (triangles), and C (stars) in $[Ln(\mathbf{L9})]^{3+}$.

(Figure 9). We observe that the correlations between the geometrical factors in solution and in the solid state are satisfying for strands A and C, but not for strand B (Figure 9), as expected from relatively large distortion from the trigonal symmetry evidenced for strand B in the solid-state structure.

We can thus build an adequate C_3-symmetrical molecular model for the averaged solution structure of $[Ln(\mathbf{L9})]^{3+}$ based either on strand A or C, which slightly differs from the crystal structure of the Eu(III) complex (Figure 10). Once a model for the solution structure is at hand, eq 9 can be used for estimating the experimental anisotropic part of the paramagnetic susceptibility tensor. Introducing the explicit expression for the isotropic part $\mathrm{Tr}\chi^j = \chi_{xx}^j + \chi_{yy}^j + \chi_{zz}^j$ together with axial symmetry $\chi_{xx}^j = \chi_{yy}^j$ for $[Ln(\mathbf{L9})]^{3+}$ into eq 9 yields

$$\delta_{ij}^{pc} = \delta_{ij}^{para} - \delta_{ij}^{c} = \frac{1}{3N_A}\left[(\chi_{zz}^j - \chi_{xx}^j)\left(\frac{3\cos^2\theta_i - 1}{r_i^3}\right)\right] \quad (20)$$

Assuming that the paramagnetic pseudo-contact contributions $\delta_{ij}^{pc} = \delta_{ij}^{para} - \delta_{ij}^{c}$ are available, a least-squares fit of eq 20 by using the geometrical factors $G_i = (3\cos^2\theta_i - 1)/r_i^3$ of the six protons H1, H5, H13, H15, H17, and H18 obtained from the C_3-symmetrical model (Figure 10) gives an estimate of the anisotropic part of the molecular axial paramagnetic susceptibility tensor $\Delta\chi^j = \chi_{zz}^j - \chi_{xx}^j$. A complete set of δ_{ij}^{pc} (Table S10, Supporting Information) can be easily obtained from δ_{ij}^{para} (Table S8, Supporting Information) and eq 7, in which δ_{ij}^{c} is calculated with eq 8 using the values of F_i collected in Table 2. However, this method is debatable because the calculation of δ_{ij}^{c} relies on the hypothesis that Bleaney's factors C_j are acceptable models for the lanthanide-based paramagnetic anisotropy, thus allowing the estimation of the contact F_i parameters, which eventually allows the recalculation of $\Delta\chi^j$ with eq 20 (Table 4, entry 1). An elegant alternative considers eq 21,[57] in which the paramagnetic anisotropies $\Delta\chi^j$ are simultaneously fitted with the contact contributions δ_{ij}^{c} by using least-squares techniques directly applied to the experimental paramagnetic lanthanide-induced chemical shifts (Table S8, Supporting Information).

$$\delta_{ij}^{para} = \delta_{ij}^{c} + \frac{1}{3N_A}\left[(\chi_{zz}^j - \chi_{xx}^j)\left(\frac{3\cos^2\theta_i - 1}{r_i^3}\right)\right] \quad (21)$$

In order to limit the number of adjustable parameters, it has been recommended to set the contact contribution to zero for nuclei separated from the paramagnetic lanthanide center by more than three chemical bonds (i.e., $\delta_{H1,j}^{c} = \delta_{H15,j}^{c} = \delta_{H17,j}^{c} = \delta_{H18,j}^{c} = 0$).[57] Consequently, for each lanthanide, six

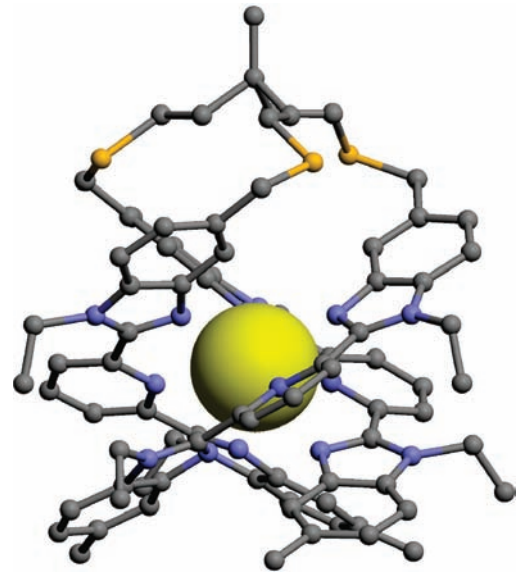

Figure 10. C_3-symmetrical model for the averaged solution structure of $[Ln(\mathbf{L9})]^{3+}$ (based on strand C, see text).

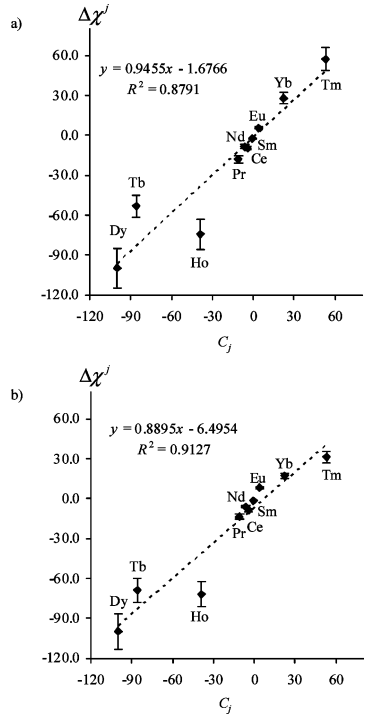

Figure 11. Plots of (a) $\Delta\chi^j$ (eq 20) versus C_j and (b) $\Delta\chi^j$ (eq 21) versus C_j for the solution structure of $[Ln(\mathbf{L9})]^{3+}$ ($\Delta\chi^j$ are scaled to $\Delta\chi^{Dy} = -100$).

equations for H1, H5, H15, H17, and H18 (eq. 21) are fitted with three parameters, $\Delta\chi^j$, δ^c_{H5}, and δ^c_{H13}, for $[Ln(\mathbf{L9})]^{3+}$ (Table 4, entries 2−4).

Both methods converge to a common set of paramagnetic anisotropies, which can be compared with Bleaney's factors (Table 4, entry 5) calculated for the free ion (Figure 11). The observed satisfying correlations of $\Delta\chi^j$ versus C_j confirm that restricting the high-temperature expansion of the susceptibility tensor to T^{-2} is an acceptable approximation for $[Ln(\mathbf{L9})]^{3+}$ podates.

Experimental Section

Chemicals were purchased from Fluka AG and Aldrich and used without further purification unless otherwise stated. The ligand **L9** and its complexes $[Ln(\mathbf{L9})](ClO_4)_3$ and $[Ln(\mathbf{L9})](CF_3SO_3)_3$ were prepared according to literature procedures.[27] $Ln(ClO_4)_3 \cdot xH_2O$ and $Ln(CF_3SO_3)_3 \cdot xH_2O$ (Ln = La−Lu) were prepared from the corresponding oxides (Aldrich, 99.99%).[58] The Ln content of solid salts was determined by complexometric titrations with Titriplex III (Merck) in the presence of urotropine and xylene orange.[59] Acetonitrile and dichloromethane were distilled over calcium hydride.

Caution! *Dry perchlorates may explode and should be handled in small quantities and with the necessary precautions.*[60,61]

Spectroscopic and Analytical Measurements. Electronic spectra in the UV−vis range were recorded at 20 °C from solutions with a Perkin-Elmer Lambda 900 spectrometer using quartz cells of 0.1 and 1 mm path lengths. Samples for NMR spectroscopy were prepared by dissolving stoichiometric amounts of **L9** and $Ln(CF_3SO_3)_3 \cdot xH_2O$ (Ln = La−Lu, 10^{-2} M) in deuterated acetonitrile at 298 K. ^1H NMR spectra were recorded on an AVANCE 400 Bruker spectrometer. The residual signal of CD_3CN was used as an internal reference, and chemical shifts are given in parts per million versus TMS. The determination of longitudinal relaxation times (T_1) used the inversion−recovery technique. The equipment and experimental procedures for luminescence measurements in the visible range were published previously.[62] Excitation of the finely powdered samples was achieved using a 300 W xenon high-pressure lamp coupled with a monochromator or a Coherent Innova argon laser. The emitted light was analyzed at 90° with a *Spex 1404* double monochromator with holographic gratings (band-pass used 0.01−0.2 nm). Emitted photon flux was measured with a *Hamatsu R-943-02* photomultiplier with a cooled CaAs(Cs) photocathode (−20 °C), coupled to a home-built linear amplifier (440 MHz) and a *Stanford Research SR-400* double photon counter. The emission spectra were corrected for the instrumental response. Luminescent lifetimes were measured using excitation provided by a Quantum Brillant Nd:YAG laser equipped with frequency doubler, tripler, and quadrupler as well as with an OPOTEK *Magic*Prism OPO crystal. Selective excitations of the 0−0 profiles were performed by means of a *Continuum MD 6000* dye laser pumped at 532 nm. The output signal of the photomultiplier was fed into a *Stanford Research SR-430* multichannel scaler and transferred to a PC. Lifetimes are averages of three independent determinations. Calculations and multilinear least-squares fits were performed with the Microsoft Excel software.

Conclusion

The replacement of methyl groups in **L10** with bulkier ethyl residues connected to the distal benzimidazole rings in **L12** (Chart 2) prevents the specific wrapping of the three strands about Eu(III), which is required for the formation of three strong intramolecular interstrand aromatic $\pi-\pi$ interactions, as observed in $[Eu(\mathbf{L10})_3]^{3+}$. A detailed analysis of the solid-state structures of $[Eu(\mathbf{L10})_3]^{3+}$ and $[Eu(\mathbf{L12})_3]^{3+}$ suggests that the main distortion concerns the relative slide of the tridentate binding units, which minimizes the steric repulsion between the ethyl groups of the different strands, a behavior reproduced in the podate $[Eu(\mathbf{L9})]^{3+}$, because of its grafting with peripheral ethyl groups. Moreover, the bond valence method evidences a concomitant increase of the Eu−N interactions in $[Eu(\mathbf{L12})_3]^{3+}$ and $[Eu(\mathbf{L9})]^{3+}$ accompanying this distortion, because of the partial relaxation of the interaromatic $\pi-\pi$ stacking interactions. High-resolution electronic excitation and emission spectra recorded in the solid state confirm the slide of the strands in $[Eu(\mathbf{L12})_3]^{3+}$ and $[Eu(\mathbf{L9})]^{3+}$, but globally speaking, these geometrical distortions remain limited and cannot explain the drop in the free energy of formation of 60−80 kJ/mol in going from $[Ln(\mathbf{L11})_3]^{3+}$ ($-133 \le \Delta G^{Ln,L11}_{1,3} \le -97$ kJ/mol) to $[Ln(\mathbf{L9})]^{3+}$ ($-46 \le \Delta G^{Ln,L9}_{1,1} \le -41$ kJ/mol) in acetonitrile.[27] Paramagnetic NMR data bring the last piece of the puzzle with the ultimate confirmation that the trigonal

(57) Forsberg, J. H.; Delaney, R. M.; Zhao, Q.; Harakas, G.; Chandran, R. *Inorg. Chem.* **1995**, *34*, 3705–3715.
(58) Desreux, J. F. In *Lanthanide Probes in Life, Chemical and Earth Sciences*; Bünzli, J.-C. G., Choppin, G. R., Eds.; Elsevier: Amsterdam, 1989; Chapter 2.
(59) Schwarzenbach, G. *Complexometric Titrations*; Chapman & Hall: London, 1957; p 8.
(60) Wolsey, W. C. *J. Chem. Educ.* **1973**, *50*, A335–A337.
(61) Raymond, K. N. *Chem. Eng. News* **1983**, *61*, 4.
(62) Rodriguez-Cortinas, R.; Avecilla, F.; Platas-Iglesias, C.; Imbert, D.; Bünzli, J.-C. G.; de Blas, A.; Rodriguez-Blas, T. *Inorg. Chem.* **2002**, *41*, 5336–5349.

wrapping of the three aromatic strands about Ln(III) in $[Ln(\mathbf{L9})]^{3+}$ nevertheless persists along the complete lanthanide series in solution. We can safely conclude that the long organic tripod is thus severely constrained upon the intramolecular coordination of the second and third tridentate binding units to the same metal, which produces a strong antichelate effect. The limited stabilities of the triple-helical mononuclear $[Ln(\mathbf{L9})]^{3+}$ podates in solution thus result from some minor improved Ln−ligand bonding interactions (including solvation effects) induced by the slide of the strands, which are largely overcome by unfavorable steric constraints occurring within the tripod. Though this balance is deleterious for the overall stability of the podates and limits their potential use as sensors or molecular devices in solution, it can be exploited for the rational design of polynuclear complexes. The unfavorable intramolecular intermetallic repulsions operating in polynuclear complexes, and which destabilize the binuclear $[Ln_2(\mathbf{L9})]^{6+}$ and trinuclear $[Ln_3(\mathbf{L9})]^{9+}$ complexes with respect to $[Ln(\mathbf{L9})]^{3+}$,[41] can be overcome by the increased number of favorable intermolecular coordination processes found in polynuclear complexes. This explains the previous unusual detection of these nonchelated binuclear $[Ln_2(\mathbf{L9})]^{6+}$ and trinuclear $[Ln_3(\mathbf{L9})]^{9+}$ complexes with heavy lanthanides in solution.[27] This concept is of broader scope than its specific application to the lanthanide podates with **L9**, and it can be considered as an additional tool for rationally controlling nuclearity in coordination complexes.

Acknowledgment. Financial support from the Swiss Office for Science and Education within the frame of the ESF COST Action D31 and from the Swiss National Science Foundation is gratefully acknowledged.

Supporting Information Available: Tables (S1−S10) and figures (S1−S5) corresponding to structural modeling and spectroscopic analyses. This material is available free of charge via the Internet at http://pubs.acs.org.

IC802130Z